LIMNOLOGY
and
OCEANOGRAPHY: METHODS

Limnol. Oceanogr.: Methods 12, 2014, 155–165

Miniature thermistor chain for determining surficial sediment porewater advection

Jonathan P. Fram[1], Geno R. Pawlak[2], Francis J. Sansone[3], Brian T. Glazer[3], and Angelos K. Hannides[3]*
[1]College of Earth, Ocean, and Atmospheric Sciences, Oregon State University, Corvallis, OR 97331
[2]Department of Mechanical and Aerospace Engineering, University of California San Diego, La Jolla, CA 92093
[3]Department of Oceanography, University of Hawai'i at Manōa, Honolulu, HI 96822

Abstract

A miniature thermistor chain (mTc) was developed to measure the subdiurnal variability of temperature in the upper layers of subtidal coastal permeable (sandy) sediments and across the sediment-water interface (SWI). The mTc has 15 precision thermistors (0.002°C accuracy) attached by narrow tines to a stainless steel backbone that connects to an electronics module, all of which is buried in the to*p* 20 cm of the sediment. Instrument performance was tested by deploying the mTc in nearshore permeable sediment at the Kilo Nalu Observatory, Oahu, Hawaii over an 80-d period. The mTc reached thermal equilibrium with the adjoining sediment within a few days after deployment and then recorded the advective propagation of the sub-daily water-column temperature variation into the sediment. The data produced are consistent with predicted effects of surface waves on advective porewater transport: transport rate increased with wave height and decreased with depth below the SWI, and temperature time lag increased with depth below the SWI. Data from an independent, more deeply buried thermistor are in good agreement with the mTc time-series data, showing attenuated temperature variability and similar (but longer, as expected) thermal time lags. Because thermal variations in surficial sediments is dominated by advection in wavy environments, mTc subdiurnal temperature propagation data can be used to calculate advective transport across the SWI and as deep as 20 cm into the sediment (i.e., over depths where advection dominates over thermal diffusion).

Surficial coastal permeable (sandy) sediments are understood to be important bioreactors in the coastal ocean (e.g., Boudreau et al. 2001; Evrard et al. 2010), and are of increasing interest to the coastal biogeochemistry community. Porewater collection and measurement techniques suitable for permeable sediments are relatively well developed (e.g., Falter and Sansone 2000; Burdige and Zimmerman 2002; Sørensen et al. 2007; Sansone et al. 2008b), whereas techniques for measuring chemical exchange (fluxes) across the sediment-water interface (SWI) are currently limited, primarily because the techniques developed for fine-grained sediments cannot be used (Boudreau et al. 2001; Rocha 2008). The latter limitation is important because the key distinguishing attribute of permeable sediments is that they are subject to significant advective transport; this advection results in enhanced water exchange between the sediment and the overlying water, rapid transport of porewater within the sediment, and transport of suspended particles from the water column to the sediment (e.g., Huettel et al. 2003).

The eddy correlation technique has been used to measure dissolved O_2 fluxes across the SWI of permeable sediments (Berg et al. 2003, 2009), but this is a difficult technique to implement at physically active field sites. Alternatively, techniques such as annular flux chambers (e.g., Glud et al. 1995) have been used to simulate sediment-seawater exchange, allowing estimation of chemical fluxes; however the accuracy of the exchange simulation under a range of conditions is not clear, limiting the utility of such measurements. Together, these limitations on the measurement of sediment-seawater fluxes have prevented the accurate assessment of the biogeochemical functioning of permeable sediments, limiting our understanding of these important systems.

The advection in wave-impacted environments predomi-

*Corresponding author: E-mail: jfram@coas.oregonstate.edu

Acknowledgments

We thank Mike Head of PME for help with design of the miniTchain instrument and for its skillful construction. We also thank Judith Wells and Brian McLaughlin for assistance in accessing and processing physical oceanographic data, and Chris Colgrove, Kimball Millikan, and Kristen Fogaren for assistance in the field. This work has been supported by the U.S. NSF (OCE-0536616 and OCE-1031947), and a Hanse-Wissenschaftskolleg Fellowship.

DOI 10.4319/lom.2014.12.155

nantly derives from wave-driven flow over seafloor sand ripples, resulting in lower pressures over sand-ripple crests than over troughs (Webb and Theodor 1968); this pressure difference infuses water into the sediment at troughs and draws water out at the crests. It can be inferred from Shum (1992), Huettel et al. (2003), and Hebert et al. (2007) that, in nearshore sands in which surface waves and currents generate clearly defined ripples, the advectively dominated layer extends to a sediment depth equal to ca. 0.5-1 sand-ripple wavelength. There are pronounced opposing gradients in dissolved oxygen and other important biogeochemical constituents at these depths (e.g., Falter and Sansone 2000; Sørensen et al. 2007; Pawlak et al. 2009), and vertical oscillations of these gradients can vary rapidly at a given site in response to changes in the physical environment (Sansone et al. 2008a; Fogaren 2010, Fogaren et al. 2013).

Precht and Huettel used dye to characterize this advective mechanism in the lab (2003) and in the field (2004), and Hebert et al. (2007) measured transport from this mechanism by injecting fluorescent dye in the field at one depth over a range of surface wave conditions. However, when Shum (1992) modeled this mechanism, he showed that transport decreased rapidly with depth within this advectively dominated layer; thus, to validate a porewater transport model of surficial permeable sediments, it is necessary to simultaneously measure transport at several depths while also accurately measuring the location of the SWI, two non-trivial tasks that are the center of interest for the work described here.

Temperature as a tracer of advective transport

After considering several alternative approaches to quantifying this depth-dependent advective transport in sands, we decided to measure sediment sub-daily temperature changes driven by the advection of overlying water (with its diurnal temperature variability) into the sediment. The water-column temperature signal should propagate through surficial sediments primarily via advective transport because diffusive processes are significantly slower in the presence of waves (e.g., Hebert et al. 2007). The temperature difference between the sediment and the overlying water column should reflect (1) the relatively long period (days-weeks) heating or cooling of the sediment by the overlying water column, generally reflecting seasonal temperature patterns, and (2) the relatively short period (hours-days) heating and cooling of the water column due to diurnal insolation (e.g., Pawlak et al. 2009, Wells et al. 2012). In addition, shorter timescale temperature changes associated with shoaling internal waves (Pawlak et al. 2009) should introduce strong gradients that propagate into the sediments.

In settings other than permeable sediments, temperature is often used to quantify transport on diurnal time scales. For example, McNeil and Farmer (1995) used water-column thermistor chains, with thermistors spaced 5 m apart, to model upper ocean mixing and transport, and to determine a diurnal dissolved oxygen budget. Diurnal heat fluxes have also been observed in intertidal sediments in which heat transport was predominantly diffusive (Thomson 2010); these experiments used a suite of independent miniature temperature recorders buried in the upper sediment. Fesker et al. (2012) described a submersible temperature probe for underwater use, but the thick body of the instrument, with its relatively large thermal mass, makes the probe unsuitable for resolving rapid processes in surficial permeable sediments.

This article describes a buried thermistor array with sensors down to ~20 cm below the SWI, a vertical sensor spacing of 1.5-2.0 cm, a low thermal conductivity, and fast response. We developed the instrument to measure advective transport, across the SWI and through the upper sediment, in subtidal coastal permeable sediments. Because temperature variation near the SWI in permeable sediments is primarily controlled by water advection, the instrument's measurement of sub-daily temperature propagation should be useful for monitoring advective transport to ~20 cm into the sediment (i.e., over depths where advection dominates over diffusion).

Materials and procedures

Miniature thermistor chain

The thermistor array and electronics package were built by Precision Measurement Engineering, and the assembly has been given the name "miniature thermistor chain" (miniTchain, mTc). The mTc electronics are based on PME's full-size thermistor chain used for water-column temperature measurement.

The mTc is comprised of 15 precision thermistors (0.002°C accuracy) attached to a 316 stainless steel backbone that connects to an electronics module (Fig. 1), all of which is buried in the top of the sediment bed. Each thermistor is potted into the end of a 9.5-cm long cylindrical tine that is constructed from a 2.5-mm diameter, 5.8-cm long Inconel tip attached to

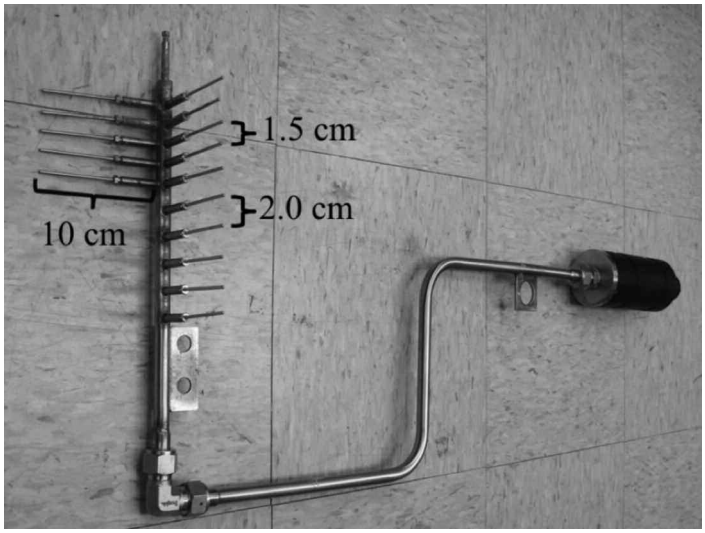

Fig. 1. Photograph of the miniTchain assembly; the black cylinder at the far right is the electronics module, with the data/power connector located at the far end; the tiles in the background are 30 × 30 cm.

a 6.6-mm diameter, 3.7-cm long stainless steel base. The tines are long and thin so that any heat conducted along the backbone of the instrument dissipates into the sediment before reaching the thermistors. Heat conduction is a concern because the thermal diffusivity of 316 stainless steel (3.5×10^{-7} m^2 s^{-1}, Engineer's Edge 2013) is higher than the diffusivity of saltwater-saturated medium/coarse sand (1.4×10^{-7} m^2 s^{-1}, Engineering Toolbox 2013).

Ten tines are aligned in a column, each oriented at a 90° angle to the backbone, with 1.5-cm spacing between the top five tines and 2.0-cm spacing between the bottom five tines. A second column of tines, with 1.5-cm spacing, is mounted along the backbone at a 90° angle to the first column of tines. The thermistors in the second column are designed to simultaneously measure temperature in the sediment at ~1/2 ripple-wavelength away from the thermistors in the first column, based on the observation that ripples at our field site generally had ~20-cm wavelengths (discussed further below).

All of the thermistors are connected to the electronics package via cables inside the 13-mm diameter 316 stainless steel backbone. The backbone has a 90° bend to minimize the amount of sand excavated to position the instrument. The electronics package converts the thermistors' analog signals into a digital serial (RS232 or RS485) ASCII string once every 100 seconds. A 2010 prototype of the mTc had the electronics package directly under the bottom thermistor, sampled every 2.5 s, and had electronics with higher power consumption; unfortunately, the heat from this electronics package created a temperature gradient comparable with the natural gradient, leading to the current instrument geometry.

For the measurements presented here, the mTc was connected to the Kilo Nalu Observatory (KNO; see below) via a 'subnode' electronics package. KNO supplied Ethernet and galvanically isolated 24-V power to the mTc subnode. The 24-V supply was grounded to seawater in the mTc to reduce noise. Data from the mTc were transmitted to an optically isolated Advantech ADAM serial-Ethernet module in the subnode.

Other instruments

Because porewater transport can be expected to change with depth in the sediment, evaluation of advective transport from the mTc data required measuring the location of the SWI with respect to the thermistors. This was done using a 650-nm, 80-mW laser with a cross-hair lens (AixiZ), which was mounted inside a Princeton Tec XL dive-light case and aimed down onto the mTc buried in the sediment; power for the laser came from the KNO infrastructure via underwater cables. The laser lines on the SWI were recorded with two 10-megapixel internet-protocol cameras (AV10005, Arecont Vision) that were mounted in custom-built PVC cases with clear acrylic endcaps. The cameras were mounted on either side of the laser, 45 cm apart, 1.20 m above the SWI, and were aimed (with a fixed focus) so that they recorded fields of view that overlapped over the mTc. Data and power connections to the KNO infrastructure were via underwater cables. The laser lines were intermittently visible by the cameras during the day, mostly visible within the hour before sunset and hour after sunrise, and clearly visible at night; image pairs were recorded every 5 min. Processing of these stereo images is described below.

A self-contained thermistor temperature logger (model TR-1060P, RBR Ltd., Kanata, Ont., Canada) measured the sediment temperature (0.002°C accuracy) independently of the mTc, 35 cm below the SWI and ~1 m alongshore of the mTc; temperatures were measured and stored every 30 seconds. A fixed water-column CTD (SBE 37, Sea-Bird Electronics) located ~8 m offshore of the mTc measured the water-column temperature (0.002°C accuracy) at a distance of ~75 cm above the SWI. KNO's acoustic Doppler current profiler (model WH 1200 kHz, Teledyne RD Instruments) and a water-column thermistor chain (PME) were used for physical oceanographic measurements; both were located ~12 m offshore of the mTc; the bottom thermistor of the thermistor chain was within 100 cm of the SWI.

Field deployment

The mTc and supporting instruments were deployed at KNO (Sansone et al. 2008a; Pawlak et al. 2009) in late January 2011 in 13-m deep water, 400 m from shore (Fig. 2) on a ~70 m wide linear sand patch set within the nearshore reef complex. The permeability of the sediment (0-20 cm) was 3.9×10^{-11} m^2 (Hannides 2008). Hebert et al. (2007) reported a homogeneous grain size distribution in the top 20 cm sediment at the same site, with 75% of grains between 125-250 μm.

The mTc was deployed by manually excavating a ~50 cm-deep hole in the sediment, positioning the instrument in the

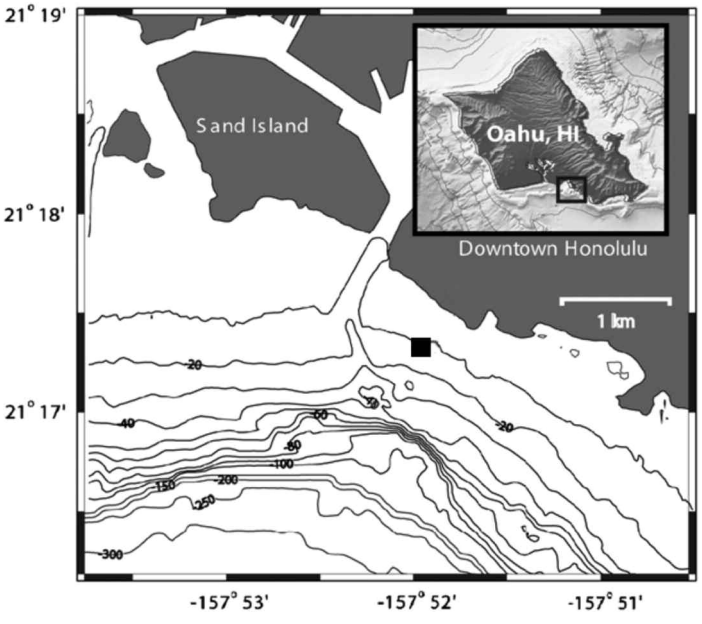

Fig. 2. Location of field site on the south shore of Oahu, Hawaii (adapted from Hebert et al. 2007). Black square indicates the sand patch where experiments were conducted. Depth contours are in meters.

hole, and then spreading the excavated sand over the instrument until the original sediment height was reestablished (Fig. 3). The mTc was deployed subsurface so it would not cause scour or otherwise interfere with sediment transport, but it was also deployed as close to the SWI as possible so it would measure porewater with the highest advection rates. Based on diver and camera observations, the surrounding sand equilibrated under typical conditions (with background wave forcing) within a few days, so that the disturbed sediment patch was indistinguishable from the surrounding area.

The stereo cameras were mounted ~1.2 m above the buried mTc on a 2-inch (5-cm) square cross-section steel beam that extended ~1 m beyond the offshore edge of a four-sided table-shaped frame made from similar beams (Fig. 4); the dimensions of the frame were 2.95 m alongshore and 1.65 m cross-shore. The experiment's subnode electronics package was mounted to a 2-m long ladder frame made of 1-inch (2.5-cm) diameter steel pipe, and this ladder frame was strapped across the top of the table frame, shoreward of the cameras and mTc. During most of this 80-d mTc deployment, we also had a 1-m high tripod and micromanipulator with electrochemical sensors located immediately onshore of the buried mTc (visible in Fig. 4). Geochemical results are outside the scope of the instrumentation described here and will be reported in a separate paper.

Data processing and analysis

Data from KN instruments were initially stored on computers in the KN shore station and were periodically synchronized with servers on campus. The significant wave height was calculated over 20-min intervals as four times the standard deviation of the ADCP-measured water level displacement time series (World Meteorological Organization 1998), and near-bed velocity magnitude was calculated as the average of the highest 1/3 of values from the bottom ADCP bin.

SWI topography data were acquired from pairs of simultaneous images using PhotoMeasure (SeaGIS). PhotoMeasure georeferenced the images and computed X, Y, and Z coordinates for selected locations visible in both images. By fitting a plane through all selected seabed points from all analyzed images, the camera's coordinate system was mapped to the seabed's, with zero height being the mean bed height and orthogonal lateral coordinates being parallel to the mean seabed. Seabed elevation was calculated over the main and off-axis thermistor columns once during each hour in which there were clear images. This was accomplished by having PhotoMeasure compute the position of six seabed points above the top of each thermistor chain. The location of the top of each thermistor column is known from the 2 days (20-21 Apr 2011) that they were both exposed. The seabed elevation at each of the thermistor columns, computed from the six points in each image pair, is

$$Z^{seabed}_{over\ mTc} = \frac{\sum_{i=1}^{6} \frac{Z_i}{(X_i - X_{mTc})^2 + (Y_i - Y_{mTc})^2}}{\sum_{i=1}^{6} \frac{1}{(X_i - X_{mTc})^2 + (Y_i - Y_{mTc})^2}} \quad (1)$$

where X is lateral distance on the seabed parallel to a line connecting the lenses of the two cameras, Y is perpendicular to X, and in the plane of the seabed, Z is normal to the plane of the

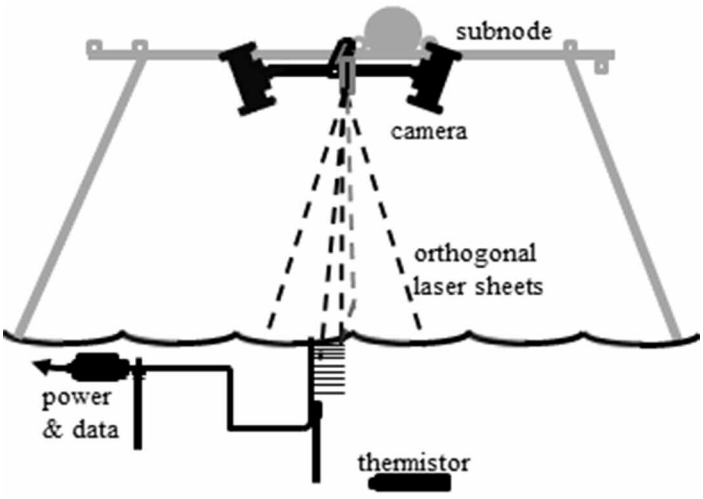

Fig. 3. Schematic diagram of miniTchain and self-contained thermistor temperature logger installed in rippled sediment. Only the main-axis thermistors are shown. Vertical metal stakes, attached to the two mounting brackets on the miniTchain, are used to keep the instrument in place during installation.

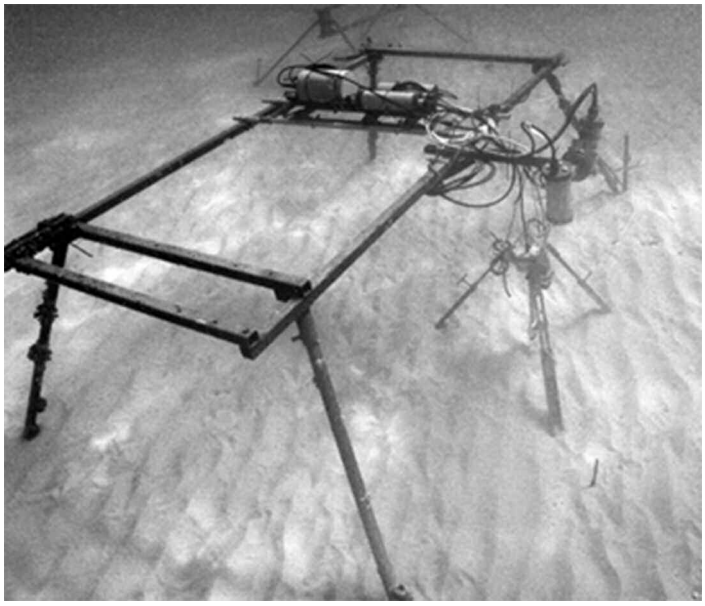

Fig. 4. Photo of the field experiment, looking alongshore; offshore is to the right. The beam extending to the right of the table-shaped main frame holds a pair of high-definition cameras. The ladder subframe, mounted across the main frame, holds the electronics package for the experiments. The miniTchain is buried underneath the temporary tripod (used for in situ chemical analyses) located below the cameras. Lasers are mounted to the tripod when it is present. Otherwise, they are mounted as in Fig. 3.

seabed, and the subscript mTc is for the location of the top the mTc's top thermistor. Laser lines crossed within a centimeter of each of the two thermistor columns, so seabed elevation could be measured day and night; however, biofouling on the camera housing obscured many images. Elevation pairs were measured during 28 Mar–6 Apr, 19 Apr–7 May, and 7-16 June 2011; 683 elevation pairs were measured during the 80-d deployment.

Ripple wavelengths on the order of 20 cm were observed from photographic images and from in situ diver observations. Estimation of ripple characteristics was attempted using subsets of image data; however, ripples were generally not regular and parallel, and so measurements were not deemed to be reliable. Alternative estimates of ripple characteristics using the model of Wiberg and Harris (1994), for the range of wave conditions observed and using a sand grain size of 200 μm (Hebert et al. 2007), yielded wavelengths of 20-25 cm at lower wave heights, diminishing to 10-12 cm for higher wave heights. Modeled ripple height were ~4 cm for low waves, diminishing to <1 cm for higher waves. These values are consistent with the observed estimates and suggest that ripple characteristics do not vary substantially at the KNO study site.

Assessment

The mTc's performance was assessed by collecting an 80-d time-series of temperature data and then analyzing four aspects of the data: 1) the equilibration of the mTc with the adjoining sediment after deployment, 2) consistency with expectations of the effects of surface waves on advective porewater transport, 3) the consistency between data from a deep-buried independent thermistor and the mTc, and 4) the lateral variations in temperature as a function of changes in sediment height due to sand ripples.

Equilibration after deployment

Immediately before the burial of the instrument on 25 Jan 2011, the sensors were isothermal to within the accuracy of the instrument (Fig. 5). After burial, it took 1-2 days for the surrounding sediment to thermally recover from the disruption, and the mTc to begin recording temperature gradients representative of those observed over the next several months. This 1-2 days equilibration time reflects the rapid rate of porewater-seawater exchange in this permeable sediment. Geochemical data from this field site (Fogaren et al. 2013) indicate that concentrations of commonly measured porewater chemical constituents also recover within a few days. Although burying the mTc could also temporarily affect porosity and permeability of the sediment, Hebert et al. (2007) suggest these physical effects would be small.

Eighty-day time-series

From late March through mid-June 2011, we collected nearly continuous temperature data from the mTc, the water-column thermistor chain, the ADCP, and the deep-buried thermistor, along with simultaneous measurements of significant surface wave height and near-bed velocity. We chose not to rebury the mTc closer to the SWI at the beginning of this period to minimize disturbance of the sand around the mTc. A gap in the water-column thermistor chain data (21-27 April) was filled with ADCP temperature data. The temperature time series are shown in Fig. 6.

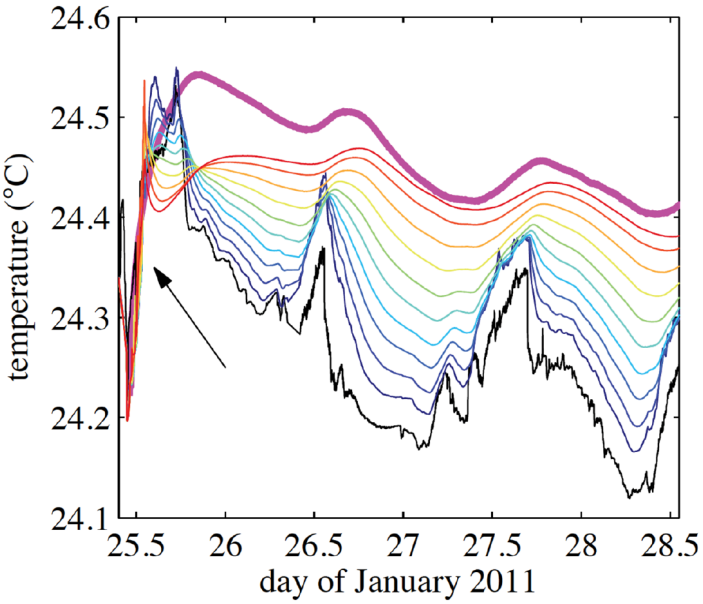

Fig. 5. Sediment temperatures recorded by the miniTchain during Jan 2011 over the 3 days immediately after insertion into the sediment, illustrating the thermal recovery rate of the sediment after burial of the instrument. See Fig. 6 for legend. Arrow indicates time when instrument was buried.

During the experiment the significant wave height, shown in Fig. 7a and Fig. 8a, ranged from 0.5 to 1.4 m, with near-bed velocities of 0.1 to 0.3 m s^{-1}. Near-bed velocity magnitude, as measured in the bottom bin of an ADCP sampling at 1 Hz, was generally dominated by wave-driven motions rather than weaker tidal velocities (<0.2 m s^{-1}), and thus followed the trends in wave height (Figs. 7a, 8a). Near-bed velocity magnitude was calculated as the mean of the highest third of measurements over 20 min, similar to significant wave height. There was a seasonal increase in all temperatures from ~24.3°C to ~25.6°C, which primarily occurred during the first half of the study (Fig. 6). Because the mTc had been buried in the sediment in late January (see next section), porewater temperatures were considered to have returned to their undisturbed state by the start of the 80-d time series in late March.

A subsample of the full time series is shown in Fig. 9, illustrating in detail the sediment temperature for May 26-31, after temperatures had stabilized from their seasonal warming. The diurnal cycle of the water-column temperature (from solar warming of the water column) is clearly seen, along with sharper changes likely associated with shoaling internal waves, as is the propagation of that temperature variation into the sediment down to at least the depth of the deepest thermistor. With increasing depths in the sediment, the amplitude

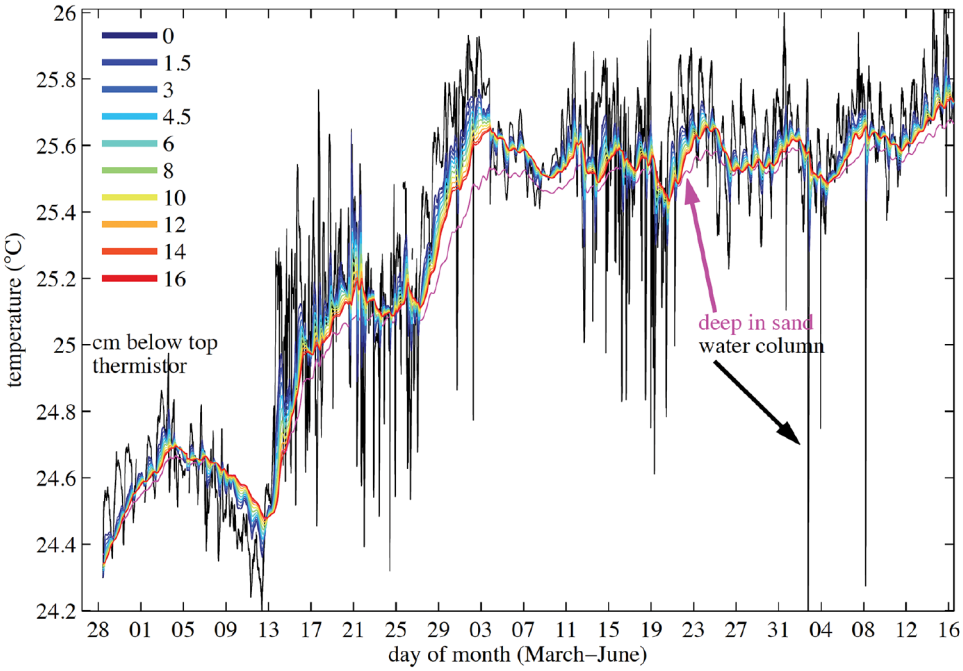

Fig. 6. Eighty-day record (March-June 2011) of mTc, self-contained thermistor temperature logger (magenta), and water-column thermistor chain temperatures (black); the sensor locations are identified in the legends.

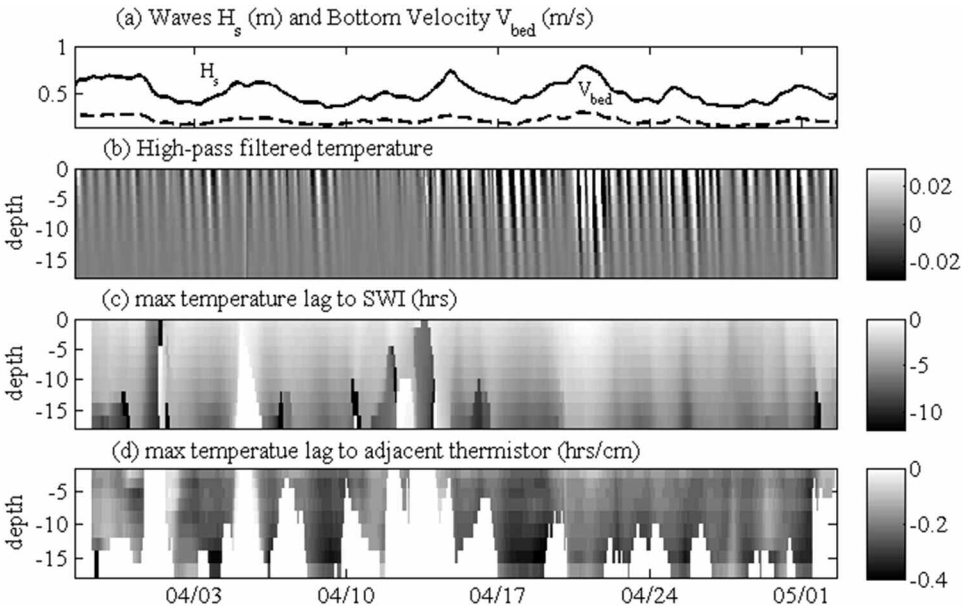

Figs. 7. Data from 28 Mar through 2 May 2011. a) Wave data are shown as a time series with a 7-interval filter (2.3 h). Solid line is significant wave height (H_s), and dashed line is near bed velocity magnitude (V_{bed}). b) High-pass (18-h) filtered temperature showing penetration of temperature signals into the sediment. c) Maximum temperature lag from the water column to each thermistor in the sediment; the smallest lag occurs near the sand-water interface. d) Change in maximum lag with depth between adjacent thermistors; the change is greater deeper in the sediment, but is also more variable, especially between the bottom two thermistors. ADCP data were not collected 3 through 12 May, so no data during that period are shown.

of the sediment temperature variation decreased and the sediment temperature increasingly lagged the water-column temperature. The median vertical temperature gradient across the mTc was 0.17°C m^{-1} over the course of the study.

Thermal propagation in the sediment

Figs. 7, 8; 10, and 11 show analyses of temperature time-lag data collected throughout the experiment. These data document the time it took for a temperature signal to propagate

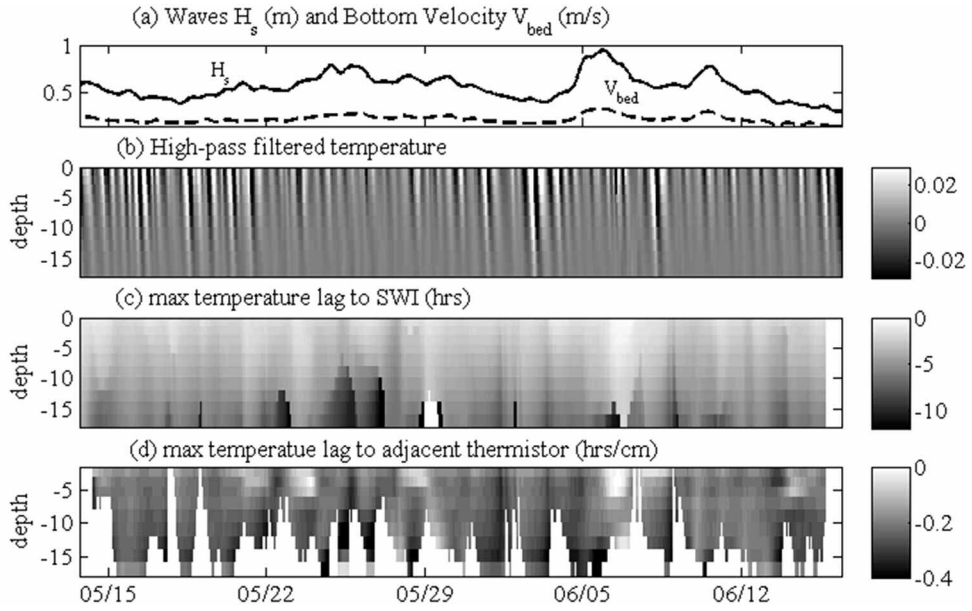

Figs. 8. Data from 13 May through 16 June 2011. a) Wave data are shown as a time series with a 7-interval filter (2.3 h). Solid line is significant wave height (H_s), and dashed line is near bed velocity magnitude (V_{bed}). b) High-pass (18-h) filtered temperature showing penetration of temperature signals into the sediment. c) Maximum temperature lag from the water column to each thermistor in the sediment; the smallest lag occurs near the sand-water interface. d) Change in maximum lag with depth between adjacent thermistors; the change is greater deeper in the sediment, but is also more variable, especially between the bottom two thermistors. ADCP data were not collected 3 through 12 May, so no data during that period are shown.

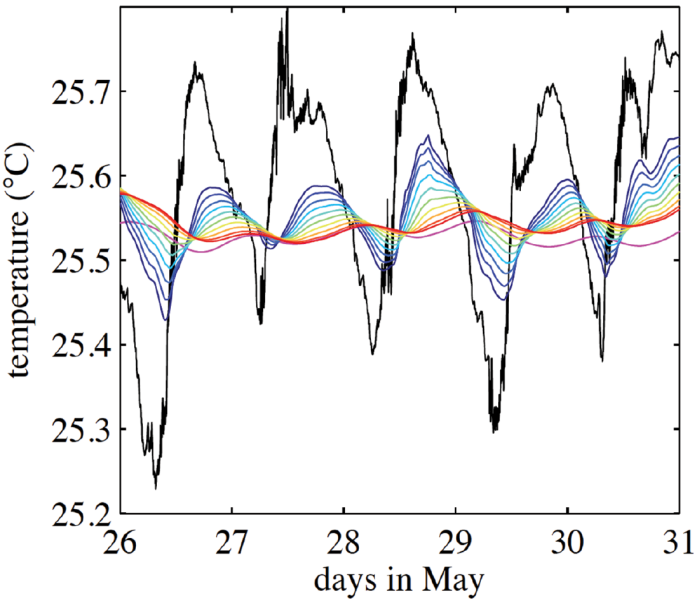

Fig. 9. Detail of temperature data collected 26-31 May 2011. The twelve colored traces show data from the ten main-axis thermistors, the self-contained thermistor temperature logger, and the water-column thermistor chain. See Fig. 6 for legend.

through the sediment, and also show the quality of mTc data.

We define the time lag (τ_{ij}) between temperature signals T_i and T_j within a given time window as the maximum of the lagged cross-covariance over all potential lags (t_{lag}):

$$\tau_{ij} = \arg_{t_{lag}} \max \left(\frac{\mathrm{cov}\left(\hat{T}_i(t),\ \hat{T}_j\left(t - t_{lag}\right)\right)}{\left\langle \hat{T}_i \right\rangle \left\langle \hat{T}_j \right\rangle} \right). \quad (2)$$

Here (^) indicates preconditioning of the temperature signal, (⟨ ⟩) represents the standard deviation over the selected time window, and t represents the time variable extending over the time window. We initially discuss lags between a buried thermistor (T_b) and the water-column thermistor (T_{wc}), $T_i = T_{wc}$ and $T_j = T_b$ with both time series conditioned (^) using an 18-h high pass filter to focus on the diurnal and faster variability.

The cross-covariances between temperatures in the water column and at each thermistor, calculated for the 80-d experiment, are shown in Fig. 10 as a function of the signal lag (t_{lag}). The time lags τ_{ij} for each thermistor represented by the location of the maxima for each curve. The results show that the shallowest (dark blue) thermistor had the best correlation with the water-column temperature (black), and had the shortest temperature time lag, and the deeper (yellow, red) thermistors sensed the water-column temperature signal with increasing time lags and lower maximum cross-covariance. During this study, it took an average of 1.2 h for the temperature signal to travel to the depth of the first thermistor (~ 7.6 cm), 2.2 h to travel to the fourth thermistor 4.5 cm below, and 6 h to travel to the bottom thermistor 11.5 cm below the fourth.

Figs. 5 and 6 show the time lags between the temperature of main-axis thermistors and to the water column temperature for the full time series. Figs. 7b and 8b show high-pass (18 h)

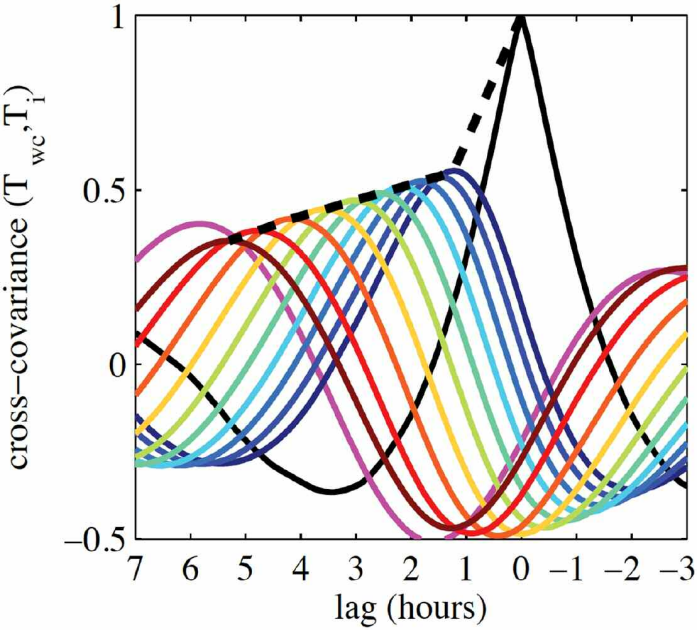

Fig. 10. Cross-covariance time lag for the March-June 2011 experiment, taken between the water-column temperature and the temperature measured by specific buried thermistors. See Fig. 6 for legend. The black dashed line connects the maximum of each curve, showing how many hours it takes for a temperature signal to reach each thermistor from the water column.

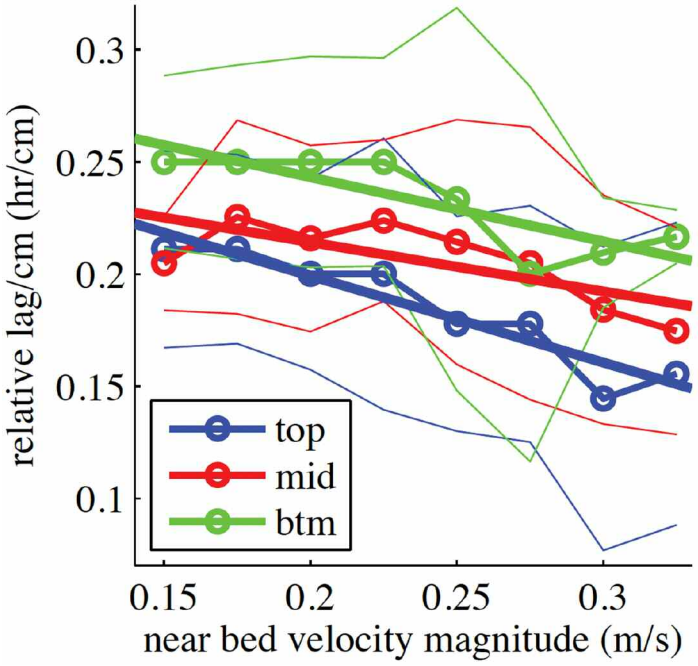

Fig. 11. The relative lag per cm between adjacent thermistors versus near bed velocity magnitude from waves for the March-June 2011 experiment. This is the reciprocal of the temperature signal's velocity into the sand. The "top" group is the median of the time lag between thermistors 1 and 2, 2 and 3, and 3 and 4 (thermistor 1 is at the top); the "middle" group is the median of the time lag between thermistors 4 and 5, and 5 and 6; the "bottom" group is the median of the time lag between thermistors 6 and 7, 7 and 8; and 8 and 9. The thin lines are standard deviations for each group. Solid lines are best fits to the median lags per cm at each wave height.

filtered temperature as a function of depth. For both positive and negative temperature differences at the SWI, the signals penetrate into the sediment over several hours, attenuating with depth. The lags between the water column and each thermistor are shown in Figs. 7c and 8c, computed over running 36-h intervals. Here the lags are calculated as defined in Eq. 2 with $T_i = T_{wc}$ and $T_j = T_b$ for each interval, with both time series preconditioned using an 18-hour high-pass filter and windowed using a Hanning function. The 18-hour filter time was selected because it is longer than the time for a signal to penetrate from the water column to the bottom thermistor and short enough to enable resolution of variability within the 36-hour window. The 36-hour interval is long enough to produce smooth results and short enough that one can distinguish variability due to wave forcing (Figs. 7a and 8a and 11).

The data in Figs. 7d and 8d are calculated in a similar manner as Figs. 7c and 8c, except that the lag is computed between adjacent thermistors ($T_i = T_k$ and $T_j = T_{k+1}$). These data shows signals slowing as a function of depth, except between the bottom two thermistors. In some periods, for the deepest thermistors, temperature variations in the water column were damped below the instrument accuracy. In these deeper regions, lag calculations between the deep thermistors and the water column (Figs. 7c and 8c) and between adjacent thermistors (Figs. 7d and 8d) were unreliable due to low cross-covariance. These regions can be seen in the sharp vertical gradients in the deeper portions in Figs. 7c and 8c. Lag data are deemed as unreliable when the maximum normalized cross-covariance between the temperature signals at each depth relative to the water column temperature is less than 0.5. This threshold was chosen to eliminate periods when data were clearly questionable, whereas maximizing data coverage. Periods with low cross-covariance mostly correspond with times of small temperature variation in the water column (e.g., 1 April) or times in which divers disturbed the site (e.g., 14 April). Data below the cross-covariance threshold, appearing in white in figures. Figs. 7d and 8d, accounted for roughly 29% of the total data, with percentages increasing with depth.

Fig. 11 collects all 70 days of data in the Figs. 7d and 8d time series to show that lag between adjacent thermistors increases with depth below the SWI and is negatively correlated with near-bed velocity magnitudes from waves, as expected from porewater advection models (e.g., Webb and Theodor 1968; Shum 1992). Lag data are grouped into top (1 to 3), middle (4 to 5), and bottom (6 to 7) thermistors. Near-bed velocity magnitude is defined as described above and shown in Figs. 7a and 8a. Larger surface waves (and correspondingly higher near-bed currents) should increase the rate of porewater-seawater advective exchange, thereby shortening

the time needed for a temperature change to propagate down through the sediment. Fig. 11 lag per distance is the reciprocal of signal speed, which in this case is porewater velocity, so another way of looking at this figure is that it shows porewater velocity increases with increasing near-bed velocity and decreases with depth below the SWI. These two trends are statistically significant in this plot. The slopes for the top and bottom lines are different from zero (P value < 0.05), whereas the slope for the middle line is not (P value = 0.11). The data for the top lines have significantly more lag/cm than the data for the middle lines (t-test P value < 0.05), and the data for the middle lines have significantly more lag/cm than the data for the bottom lines. These data are plotted against near bed velocity magnitude (V_{bed}), but results are similar for these data plotted against significant wave height (H_s) (not shown), consistent with the fact that the near-bed velocity is primarily correlated with surface waves, with only weak contributions from tidally driven flow and other low frequency sources.

The local lag values in Fig. 11 are consistent with the estimates in Fig. 10, considering that the latter are based on integrated transport to the depth of each sensor, which will be faster than local transport rates at a given depth. Data from the independent, deep-buried thermistor are consistent with those from the mTc. For example, in Figs. 6 and 9 the deep thermistor showed attenuated temperature variability, as compared width the shallower mTc thermistors, although with similar (but longer, as expected) thermal time lags (Fig. 10).

Extrapolating porewater velocities from Fig. 11 to the sediment surface to estimate surface porewater fluxes gives values of 6-11 cm/h, (depending on V_{bed},) with a mean of 7.6 cm/h. These values are consistent with those found by others using different methods (Table 1 from Hebert et al. 2007), and over an order of magnitude higher than typical porewater velocities from subtidal submarine discharge (Burnett et al. 2006). These velocities can be used with geochemical concentrations (and porosity) to estimate geochemical surface fluxes.

Lateral variations in temperature

The mTc design included a set of thermistors aligned along a secondary axis to allow investigation of lateral variations in temperature. It was expected that temperature would vary depending on where the measurements were taken with respect to the ripple crests and troughs at the sediment surface because of differences in the direction of porewater flow (e.g., Shum 1992); it was further expected that the location of the two thermistor axes with respect to ripples and crests could be monitored by measuring the sediment height above each axis at the time of each temperature measurement. However, no measurable temperature difference was observed between the two axes as a function of SWI height. The lack of appreciable lateral gradients may be a result of inaccuracies in SWI measurement or effects of complex 3D ripple fields often observed at the field site (cf. Fig. 4). One source of inaccuracy is associated with possible motion of the camera mount due to waves. The cameras may have moved with respect to each other in May, which would explain why the sediment depths of the two thermistor chains are generally offset in June, but not in March or April (Fig. 12). In addition, crest versus trough temperature differences might have been more evident if the mTc had been deployed closer to the SWI. The top thermistor on each column was located at an average depth of 7.6 cm below the SWI, but could have been deployed about 4 cm closer to the SWI without being exposed regularly under ripple troughs.

Conclusions and recommendations

The mTc reached equilibration with the adjoining sediment within a few days after deployment (Fig. 5), and produced data that are consistent with expected effects of surface waves on advective porewater transport (e.g., Fig. 11). The field data show that the mTc is able to monitor porewater transport through the depths of interest in surficial permeable sediments

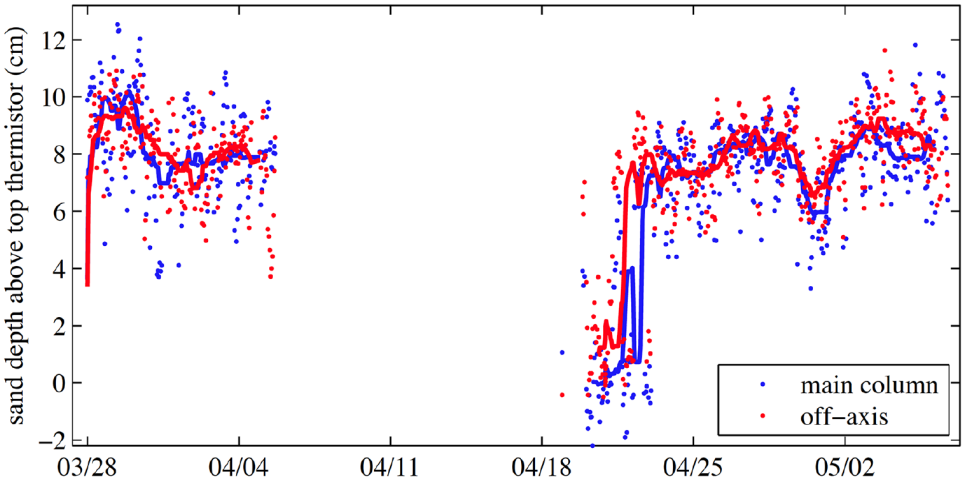

Fig. 12. Sand depth above the top thermistor of each of the two vertical columns of thermistors on the miniTchain during the March-June 2011 experiment.

underlying water-columns with sub-daily temperature oscillations of a least a few tenths of a degree C. The depth over which porewater transport can be estimated for a given location will depend on the scale of the temperature fluctuations, the sediment's thermal diffusivity, and the measurement accuracy. For temperature fluctuations observed at KNO, we estimate that the mTc data can be used to calculate advective porewater transport to at least 20 cm into the sediment.

One limitation of the mTc is that its measurements are highly dependent upon accurately coregistering the location of the SWI above the instrument with respect to ripple migration. There are a number of ways to measure burial depth of the mTc, but all methods we have considered either lack sufficient resolution (e.g., acoustic altimeter), introduce disturbance (e.g., profiling resistivity sensors), or are prohibitively expensive (e.g., LIDAR). The difficulty in measuring the height of the SWI without disturbing the interface is a major reason for the use of stereo photography described here, despite the intensive data processing required.

Another challenge is that the mTc should be buried as close to the SWI as possible (because that is where the largest temperature gradients are) without exposing it to the water column (which could affect sand erosion/deposition patterns and thus the SWI surface pressure gradients that drive the porewater advection that we aim to measure). Thus, the burial depth needs to reflect the dynamics of each field site, with a deeper burial depth in more physically active environments.

Also, the mTc can be used in surficial permeable sediments only where the water column temperature near the SWI changes on time scales similar to the time scales of the porewater advection one wants to monitor. At our field site, there is an insolation-driven diurnal temperature signal because it is located above the diurnal thermocline. In more turbid waters, a solar signal might not be available, but there may be internal waves that provide sufficient benthic temperature changes at regular tidal intervals (e.g., Fram et al. 2008). Whereas we demonstrated this instrument in coastal sediment, it may have application elsewhere, such as the hyporheic zone in river beds (e.g., Stanford and Ward 1988). Although the focus of the present paper is on using the mTc to measure permeable sediment porewater advection, the instrument could also be used for measurements of long-term thermal diffusion in fine-grain sediments, which is related to properties such as porosity and sediment composition (e.g., Thomson 2010).

Although we used the mTc in combination with a cabled underwater observatory (for data retrieval and power), the instrument could be modified to allow autonomous operation. This would require that the electronics module be fitted with internal data storage and a small battery.

Advective porewater transport, as modeled by Shum (1992), decreases approximately exponentially with depth, and the mTc can be used down to the lowest depth below the SWI at which heat transport from thermal diffusion is comparable to the advective transport. The mTc is limited to permeable sediments for measuring advection because advective transport in fine-grain sediments dominates only on the scale of millimeters (Huettel et al. 2003), and about one centimeter is the minimum thermistor spacing for a mTc made with the components described here. These limitations leave a large area where this instrument may be useful because permeable sediments cover much of the coastal shelf (e.g., Boudreau et al. 2001), and much of the recycling of coastal water-column nutrients occurs in the advection-dominated region of permeable sediments (Huettel et al. 1998).

Finally, models of advective transport in rippled surficial permeable sediments, using Darcy's Law and estimates of the SWI pressure distribution, have been developed by Shum (1992) and Cardenas et al. (2008); however, the calculated porewater velocities from these models have not been quantitatively validated, primarily due to the lack of field data on porewater transport rates. The mTc should be able to provide useful data for such model verification.

References

Berg, P., H. Røy, F. Janssen, V. Meyer, B. B. Jørgensen, M. Huettel, and D. de Beer. 2003 Oxygen uptake by aquatic sediments measured with a novel noninvasive eddy-correlation technique. Mar. Ecol. Prog. Ser. 261:75-83 [doi:10.3354/meps261075].

———, R. N. Glud, A. Hume, H. Stahl, K. Oguri, V. Meyer, and H. Kitazato. 2009. Eddy correlation measurements of oxygen uptake in deep ocean sediments. Limnol. Oceanogr. Methods 7:576-584 [doi:10.4319/lom.2009.7.576].

Boudreau, B. P., and others. 2001. Permeable marine sediments: overturning an old paradigm. Eos Trans. Am. Geophys. Union 82:133-136.

Burnett, W. C., and others. 2006. Quantifying submarine groundwater discharge in the coastal zone via multiple methods. Science Total Environ. 367:498-543 [doi:10.1016/j.scitotenv.2006.05.009].

Burdige, D. J., and R. C. Zimmerman. 2002. Impact of sea grass density on carbonate dissolution in Bahamian sediments. Limnol. Oceanogr. 47:1751-1763 [doi:10.4319/lo.2002.47.6.1751].

Cardenas, M. B., P. L. M. Cook, H. Jiang, and P. Traykovski. 2008. Constraining denitrification in permeable wave-influenced marine sediment using linked hydrodynamic and biogeochemical modeling. Earth Planet. Sci. Lett. 275:127-137 [doi:10.1016/j.epsl.2008.08.016].

Engineer's Edge. 2013. Thermal properties of metals, conductivity, thermal expansion, specific heat. <http://www.engineersedge.com/properties_of_metals.htm>.

Engineering Toolbox. 2013. Thermal conductivity of common materials. <http://www.engineeringtoolbox.com/thermal-conductivity-d_429.html>.

Evrard, V., K. Soetaert, C. H. R. Heip, M. Huettel, M. A. Xenopoulos, and J. J. Middelburg. 2010. Carbon and nitrogen flows through the benthic food web of a photic subti-

dal sandy sediment. Mar. Ecol. Prog. Ser. 416:1-16 [doi:10.3354/meps08770].

Falter, J. L., and F. J. Sansone. 2000. Hydraulic control of pore water geochemistry within the oxic-suboxic zone of a permeable sediment. Limnol. Oceanogr. 45:550-557 [doi:10.4319/lo.2000.45.3.0550].

Fesker, T., G. Wetzel, and B. Heesemann. 2012. Introducing the T-Stick: A new device for high precision in situ sediment temperature profile measurements. Limnol. Oceanogr. Methods 10:31-40 [doi:10.4319/lom.2012.10.31].

Fogaren, K. E., F. J. Sansone, and E. H. DeCarlo. 2013. Porewater temporal variability in a wave-impacted permeable nearshore sediment. Mar. Chem. 149:74-84 [doi:10.1016/j.marchem.2012.12.005].

———, 2010. Short-time Scale and Seasonal Variability of Porewater Constituents in a Permeable Nearshore Sediment. M.S. Thesis, University of Hawaii at Manoa, Honolulu, 86 pp.

Fram, J. P., H. L. Stewart, M. A. Brzezinski, B. Gaylord, D. C. Reed, S. L. Williams, and S. Macintyre. 2008. Physical pathways and utilization of nitrate supply to the giant kelp, *Macrocystis pyrifera*. Limnol. Oceanogr. 53:1589-1603 [doi:10.4319/lo.2008.53.4.1589].

Glud, R. N., J. K. Gundersen, N. P. Revsbech, B. B. Jorgensen, and M. Huettel. 1995. Calibration and performance of the stirred flux chamber from the benthic lander Elinor. Deep-Sea Res. I 42:1029-1042 [doi:10.1016/0967-0637(95)00023-Y].

Hannides, A. K. 2008. Organic matter cycling and nutrient dynamics in marine sediments. Ph.D. dissertation, Univ. Hawaii at Manoa, Honolulu.

Hebert, A. J., F. J. Sansone, and G. R. Pawlak. 2007. Tracer dispersal in sandy sediment porewater under enhanced physical forcing. Cont. Shelf Res. 27:2278-2287 [doi:10.1016/j.csr.2007.05.016].

Huettel, M., W. Ziebis, S. Forster, and G. W. Luther. 1998. Advective transport affecting metal and nutrient distributions and interfacial fluxes in permeable sediments. Geochim. Cosmochim. Acta 62:613-631 [doi:10.1016/S0016-7037(97)00371-2].

———, H. Roy, E. Precht, and S. Ehrenhauss. 2003. Hydrodynamical impact on biogeochemical processes in aquatic sediments. Hydrobiologia 494:231-236 [doi:10.1023/A:1025426601773].

McNeil, C. L., and D. M. Farmer. 1995. Observations of the influence of diurnal convection on upper ocean dissolved gas measurements. J. Mar. Res. 53:151-169 [doi:10.1357/0022240953213313].

Pawlak, G., and others. 2009. Development, deployment, and operation of Kilo Nalu Nearshore Cabled Observatory, p. 1–10. *In* IEEE Oceans '09, Bremen, Germany. IEEE [doi:10.1109/OCEANSE.2009.5278149].

Precht, E., and M. Huettel. 2003. Advective pore-water exchange driven by surface gravity waves and its ecological implications. Limnol. Oceanogr. 48:1674-1684 [doi:10.4319/lo.2003.48.4.1674].

———, and M. Huettel. 2004. Rapid wave-driven advective pore water exchange in a permeable coastal sediment. J. Sea Res. 51:93-107 [doi:10.1016/j.seares.2003.07.003].

Rocha, C. 2008. Sandy sediments as active biogeochemical reactors: compound cycling in the fast lane. Aquat. Microb. Ecol. 53:119-129 [doi:10.3354/ame01221].

Sansone, F. J., and others. 2008a. Kilo Nalu: Physical/ biogeochemical dynamics above and within permeable sediments. Oceanography 21:120-125 [doi:10.5670/oceanog.2008.15].

———, H. L. Spalding, and C. M. Smith. 2008b. Submersible-operated porewater sampler for sandy sediments. Limnol. Oceanogr. Methods 6:119-125 [doi:10.4319/lom.2008.6.119].

Shum, K. T. 1992. Wave-induced advective transport below a rippled water-sediment interface. J. Geophys. Res. 97:789-808 [doi:10.1029/91JC02101].

Sørensen, K, B. T. Glazer, A. Hannides, and E. Gaidos. 2007. Spatial structure of the microbial community in sandy carbonate sediments. Mar. Ecol. Progr. Ser. 346:61-74 [doi:10.3354/meps06996].

Stanford, J. A., and J. V. Ward. 1988. The hyporheic habitat of river ecosystems. Nature 335:64-66 [doi:10.1038/335064a0].

Thomson, J. 2010. Observations of thermal diffusivity and a relation to the porosity of tidal flat sediments. J. Geophys. Res. 115:C05016 [doi:10.1029/2009JC005968].

Webb, J. E., and J. Theodor. 1968. Irrigation of submerged marine sands through wave action. Nature 220:682-683 [doi:10.1038/220682a0].

Wells, J. R., J. P. Fram, and G. Pawlak. 2012. Solar warming of near bottom water over a fringing reef. J. Mar. Res. 70:641-660 [doi:10.1357/002224012805262734].

Wiberg, P. L., and C. K. Harris. 1994. Ripple geometry in wave-dominated environments. J. Geophys. Res. 99:775-789 [doi:10.1029/93JC02726].

World Meteorological Organization. 1998. Guide to wave analysis and forecasting. World Meteorological Organization. 168 pp.

Submitted 29 July 2013
Revised 3 January 2014
Accepted 13 March 2014